Reconstructing Synoptic Maps of Solar Wind Radial Velocity between 20 and 60 $R_\odot$ Based on STEREO/HI1 Images

Xiaolei Li[1,2], Yuming Wang[1,2], Fang Shen[3], Yi Yang[3], Quanhao Zhang[1,2], and Shaoyu Lyu[1,2]

[1] Deep Space Exploration Laboratory/School of Earth and Space Sciences, University of Science and Technology of China, Hefei 230026, People's Republic of China; ymwang@ustc.edu.cn

[2] CAS Center for Excellence in Comparative Planetology/CAS Key Laboratory of Geospace Environment/Mengcheng National Geophysical Observatory, University of Science and Technology of China, Hefei 230026, People's Republic of China

[3] SIGMA Weather Group, State Key Laboratory of Space Weather, Center for Space Science and Applied Research, Chinese Academy of Sciences, Beijing 100190, People's Republic of China

Abstract

Previously, we developed a correlation-aided reconstruction method to recognize and locate solar wind transients observed by the Heliospheric Imager-1 (HI1) on board the Solar Terrestrial Relations Observatory and then developed a technique to infer the radial velocity distribution in each solar wind transient. Considering that the common field of view of HI1 may cover the full longitudes through the solar rotation, we further apply these methods to small-scale transients (STs) in a complete Carrington rotation to reconstruct a synoptic map of the solar wind radial velocity. Our test suggests that the reconstructed synoptic map is in agreement with the preset synthetic STs in latitude, longitude, and radial velocity. Then, Carrington rotation 2095 between 2010 March 26 and April 22 is selected to demonstrate the new technique. The derived synoptic map shows that the solar wind radial velocity corresponding to STs is in the range of 250–550 km s^{-1} between 20 and 60 $R_\odot$ in the low-to-middle latitudes. We extrapolate the in situ observation near 1 au to 20 $R_\odot$ and find that it matches the synoptic velocity map well. The magnetohydrodynamic simulations of the solar wind radial velocity are consistent with the synoptic map near the heliospheric current sheet (HCS) but usually overestimate the velocity values for STs far away from the HCS. We expect that this technique will be a powerful tool to learn about and monitor the solar wind in the inner heliosphere, where the number of human probes is limited.

Unified Astronomy Thesaurus concepts: Solar wind (1534)

Supporting material: animations

1. Introduction

Solar wind, as magnetized plasma originating from the solar corona, floods the heliosphere and continually impacts the space environment of the planets and spacecraft therein. Different from the fast solar wind (>500 km s^{-1}) originating from large coronal holes (Hollweg & Isenberg 2002), the slow solar wind (<500 km s^{-1}) comes from the loops around the helmet streamers and the heliospheric current sheet (HCS; Stakhiv et al. 2016) or from the pseudostreamers (Crooker et al. 2012) with a latitudinal extending range of about 40°–60° in solar minimum around the HCS (McComas et al. 2008). Once propagating out, the solar wind keeps accelerating in the corona, and the acceleration falls to almost zero in the heliosphere. Due to the solar rotation, the magnetic field line carried by the solar wind in the heliosphere evolves as an Archimedes screw, called the Parker spiral (Parker 1958).

The observation of the solar wind velocity, especially at heliocentric distances close to the Sun, plays the key role in tracing the origin of different kinds of solar wind and forecasting of space weather in the heliosphere. The knowledge of the near-Sun solar wind velocity may either depend on in situ observations by spacecraft like the Parker Solar Probe (PSP), with a minimum perihelion of no more than 10 $R_\odot$ (Kasper et al. 2016), or rely on three-dimensional (3D) reconstruction from global remote-sensing observations like interplanetary scintillation (IPS) measurements or stereoscopic white-light imaging by coronagraphs or heliospheric imagers. By applying the computer-assisted tomography technique on IPS from different radio sources, the 3D velocity map can be reconstructed in relatively low temporal and spatial resolution (Jackson et al. 1998; Tokumaru et al. 2021). On the other hand, variation of Thomson-scattering light from solar wind plasma density variation can be recorded by spaceborne white-light imagers like the coronagraphs (COR1 and COR2) and heliospheric imagers (HI1 and HI2) in the Sun Earth Connection Coronal and Heliospheric Investigation (SECCHI) suite (Howard et al. 2008) on board the Ahead/Behind Solar Terrestrial Relations Observatory (STEREO-A/B). Combining visible-light images and coronagraphic HI Lyα ultraviolet (UV) observations can help map the solar wind flow velocity at a heliocentric distance of less than 4 $R_\odot$ (Dolei et al. 2018; Capuano et al. 2021). Without UV observations, wide-field white-light images with high cadence and pixel resolution can still be used to infer the solar wind velocity remotely if suitable solar wind tracers such as small-scale transients are observed (e.g., Sheeley et al. 1997; Rouillard et al. 2010; Plotnikov et al. 2016; Li et al. 2021).

Small-scale transients (STs) can be widely observed in the solar wind outflows as macroscopic plasma density perturbation (DeForest et al. 2018). Some STs, called blobs, have a clear circular or oval shape (Rouillard et al. 2010; Sanchez-Diaz et al. 2017a), while some, called flocculae, look like fading puffs (DeForest et al. 2016). Many STs are emitted from
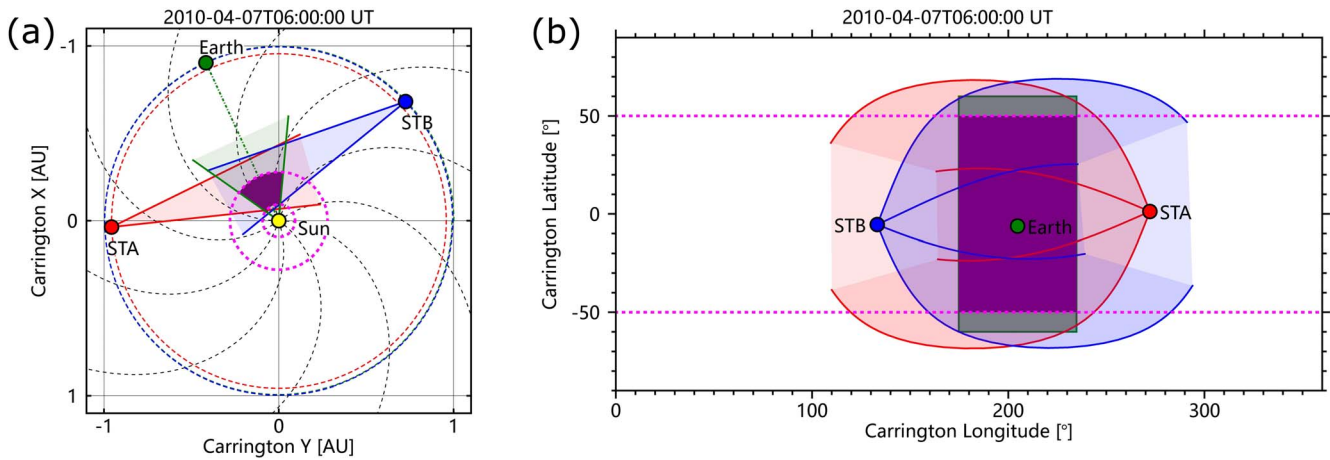
Figure 1. Position of STEREO-A/B (red/blue), Earth (green), and the Sun (yellow) on the equatorial plane (a) or in the angular space (b) during CR 2095 in Carrington coordinates. The blue and red semitransparent regions represent the FOV for HI1 on board STEREO-A/B. The green semitransparent region marks the space for reconstructed transients at the current frame. The purple region is where the solar wind velocity and position data are derived for sampling at each time frame. On the equatorial plane (panel (a)), the black dashed curves represent the Parker spiral with a radial solar wind velocity of 450 km s^{-1}, while the Sun–Earth line is marked as a green dashed–dotted line. The orbits of Earth and STEREO-A/B are plotted as green, red, and blue dashed circles, respectively. The two thick magenta dashed circles in panel (a) at heliocentric distances of 20 and 60 $R_\odot$ represent the inner and outer boundaries of the sampling grids, while the two thick magenta dashed lines in panel (b) at latitudes of 50°N and 50°S represent the latitudinal upper and lower boundaries of the sampling grids. A corresponding animation of panels (a) and (b) during the full CR 2095 is provided in the online journal. It covers about 27 days in CR 2095 from 12:00 UT on 2010 March 26 to 18:00 UT on 2010 February 22. The video duration is 3 s.

(An animation of this figure is available.)

the Sun at a period from 2.5 to several tens of hours (Viall et al. 2010; Viall & Vourlidas 2015). Different from large-scale transients like shocks or coronal mass ejections (CMEs) that continue interacting with the background solar wind, STs propagate out along with the ambient solar wind after origination at the high corona resulting from interchange reconnection and tearing instability (Sanchez-Diaz et al. 2017b; Réville et al. 2020). Thus, they are considered as ideal tracers of the ambient solar wind to infer the solar wind velocity (Sheeley et al. 1997; López-Portela et al. 2018). Due to the solar rotation and magnetic freezing of the solar wind plasma, all of the STs from the same source region with the same radial velocity align on the same Parker spiral (Sheeley et al. 2008) and are called corotating density structures if embedded in the solar wind compressed region (Plotnikov et al. 2016).

Many methods have been used to reconstruct the solar wind velocity based on ST white-light images. By fitting the J-shaped bright traces of transient fronts on the time-elongation map (called the J-map), the local solar wind velocity and position of the ST source region can be precisely derived (e.g., Plotnikov et al. 2016). By analyzing imaging data at neighboring frames (e.g., Ying et al. 2019) or applying Fourier motion filters to white-light images in a long period of time (e.g., Cho et al. 2018), many methods are developed to plot the global two-dimensional (2D) map of the solar wind velocity component on the sky plane (the plane perpendicular to the line of sight).

Recently, we (Li et al. 2020, hereafter Paper I) developed a technique called the correlation-aided reconstruction (CORAR) method to identify the positions of all of the transients imaged by STEREO-A/B Heliospheric Imager-1 (HI1), and we further (Li et al. 2021, hereafter Paper II) generated a 2D map of the radial velocity of all of the transients in the images, and name the corresponding method maximum correlation-coefficient localization and cross-correlation tracking (MCT). With the aid of these techniques, in this paper, we try to build a synoptic map of the solar wind radial velocity at the heliocentric

distance between 20 and 60 $R_\odot$ by tracing all of the STs in a Carrington rotation (CR). In Section 2, we introduce the instruments and data. The method used to construct the synoptic solar wind map and an example of a test with synthetic images of STs are described in Section 3. In Section 4, we apply this method to STEREO/HI1 observations during CR 2095 and compare our results with a magnetic neutral line at 2.5 $R_\odot$, in situ observations at 1 au, and solar wind simulations. The last section is the summary and conclusions.

2. Instruments and Data

The STEREO-A/B spacecraft have similar orbits around the Sun as the Earth on the ecliptic plane, but their separation angle to the Earth has increased about 22.5° every year since their launch into space in 2006 (Harrison et al. 2008). On board the STEREO spacecraft, HI1 normally continually images the heliosphere at a cadence of 40 minutes. It has a pixel resolution of 1024 × 1024 in a field of view (FOV) of 20° × 20° with its center at an elongation angle of 14° on the ecliptic plane (Eyles et al. 2009).

In this paper, we select CR 2095, which is from 2010 March 26 to April 22, to demonstrate the synoptic solar wind map. One of the reasons is that the two STEREO HI1 have a large common FOV with a separation angle about the Sun of around 140° (see Figure 1), which is suitable for solar wind small-scale transient reconstruction (Paper I; Lyu et al. 2021). Another reason is that it stays in the ascending phase of the solar cycle when there are fewer large-scale transients like CMEs to contaminate the images of STs compared to solar maximum.

From the STEREO Science Center, we get the level 2 HI1 data in which 1 day background emission, defined as the average of the lowest 25% of the data in a running window of 1 day on a pixel-by-pixel basis, is cleared away. Then, we preprocess it by deriving its shifted running difference and

3×3 median smoothing to keep the pure transient patterns (see Paper I for more details).

3. Method

The reconstruction of the synoptic solar wind map first relies on the identification, location, and local velocity derivation of all of the STs in the common FOV of two white-light images (blue and red semitransparent regions in Figure 1). In a solar corotating coordinate system, like Carrington coordinates, the common FOV would make a full 360° coverage in longitude in one CR due to the solar rotation (see supporting material, M1. mp4). By assembling the derived solar wind radial velocities in these common FOVs, we get the synoptic map.

3.1. Procedures

Procedure 1: Derivation of the STs' position and velocity. At each frame, we apply the CORAR method (Paper I) to build the 3D correlation coefficient (cc) map of the transients observed by STEREO-A/B. Based on the 3D cc map, we use the MCT method (Paper II) to derive the spatial distribution of the probable 3D position and radial velocity distribution of the transients on the original images (displayed in Figure 2(a)). The basic parameters of the CORAR method and MCT technique are the same as in Papers I and II, but we decrease the longitudinal range of the 3D cc map from $(-60°, 60°)$ to $(-30°, 30°)$ in heliospheric Earth ecliptic coordinates (see the green semitransparent region between the two green lines in Figure 1) and reduce the temporal sampling-box length from 5 to 3 to increase the computational efficiency. Note that only the STs are reasonable tracers of the solar wind embedded in them, so we manually exclude the data when CMEs appear in the HI1 images.

Procedure 2: Data assembling. We generate uniform grids in 3D (r, ϕ, λ) (heliocentric distance–latitude–longitude) space with an r range of $(20, 60 \, R_\odot)$, a ϕ range of $(0°, 360°)$, a λ range of $(-50°, 50°)$, and grid spacing of $(1 \, R_\odot, 1°, 1°)$. At each time frame, the position of each ST data point is transformed into Carrington coordinates. After collecting all of the ST data points in a CR, we count the points within each grid. If the number of ST data points within a grid is large enough ($\geqslant 10$), we calculate their median value, v_s, and the standard deviation, δv_s, to the median value. Otherwise, the velocity associated with the grid is invalid. Finally, all of the valid velocity data are assembled to form a synoptic solar wind velocity map (see Figure 2(b)).

Procedure 3: Data smoothing, extension, and denoising. Due to missing data or a lack of identification of some transients at some time frames, the velocity map from procedure 2 is usually fragmented; in particular, it is not continuous along the Parker spiral. We fix and smooth the fragments along the Parker spiral by assuming that the ambient solar wind from the same source region aligns along the same Parker spiral magnetic field line determined by a constant solar wind velocity, as shown in Figure 2(c). Then, we remove the tiny structures as probable noise generated in the previous procedures to derive the final synoptic solar wind velocity map (see Figure 2(d)). A detailed description of this procedure is given in the Appendix.

3.2. Test with Synthetic Images

We create the synthetic STEREO HI1 images to test the accuracy of the synoptic velocity map reconstruction. First, at a heliocentric distance of $20 \, R_\odot$, we build 10 source regions of STs randomly distributed in angular space with the solar wind velocity randomly distributed in the range between 100 and $800 \, \mathrm{km \, s^{-1}}$, as Figure 3(a) shows. For each source region, we set the transient emitting time interval to randomly range from 2.5 to 20 hr according to the observational frequency of the periodic density structures in the HI1 images (Viall et al. 2010; Sanchez-Diaz et al. 2017a). The spherical blob model is used to simulate the ST's density distribution (see Chapter 3.1 of Paper I for details). As a transient radially propagates, the ball is set to self-similar expand, so its half-angular width to the Sun, α, stays the same, and the central plasma density, n_c, decays cubically with heliocentric distance. For different transients, we set α to be randomly distributed from 2° to 5°, and the range of the initial n_c is between 10^2 and $10^4 \, \mathrm{cm^{-3}}$. Based on the density distribution of the reconstructed transients at each frame, their Thompson scattering brightness pixel by pixel for each HI1 on board STEREO-A/B is calculated and added to the background images, as we did in Paper I to create the synthetic HI1 images. Applying the techniques described in Section 3.1 to the synthetic images, we build the synoptic velocity map.

The inferred velocity distribution of the source regions at a heliocentric distance of $20 \, R_\odot$ is shown in Figure 3(b). We compared the Carrington longitude, latitude, and velocity (v_r) between the prearranged synthetic source regions and the reconstructed source regions in the synoptic velocity map (Figures 3(c)–(e)). It shows that they are highly coincident with each other. Their mean absolute deviation is only 1°.0 in centering Carrington longitude, 0°.7 in centering Carrington latitude, and $4 \, \mathrm{km \, s^{-1}}$ in velocity, which means that the reconstruction technique can infer the solar wind velocities of the STs with high precision.

4. Synoptic Solar Wind Velocity Map of CR 2095

We apply our method to real STEREO HI1 images during CR 2095 and reconstruct the synoptic solar wind velocity map at a heliocentric distance between 20 and $60 \, R_\odot$. Figures 4(a)–(c) show the synoptic maps cutting a latitude of 20°S, longitude of 75° (or 225°), and heliocentric distance of $30 \, R_\odot$. Figure 4(e) displays the 3D view of the synoptic velocity map (see the online journal for the animated version). The solar wind embedding small-scale transients spreads widely in angular space and varies from 240 to more than $500 \, \mathrm{km \, s^{-1}}$ in velocity.

The distribution of the reconstructed solar wind velocity is shown in Figure 4(d). One major peak appears around 310 $\mathrm{km \, s^{-1}}$, and another minor peak appears around $400 \, \mathrm{km \, s^{-1}}$. The major one is in good agreement with the velocity distribution peak and the mean value of the corotating density structure in the STEREO-A HI J-map on the ecliptic plane (Plotnikov et al. 2016). The minor one mainly corresponds to the part of the velocity map at a Carrington longitude between 240° and 300° at higher latitudes ($\sim$20°; see Figure 4(c)). The variation of the inferred velocity in the 3D space suggests a complication of the solar wind distribution in the inner heliosphere.
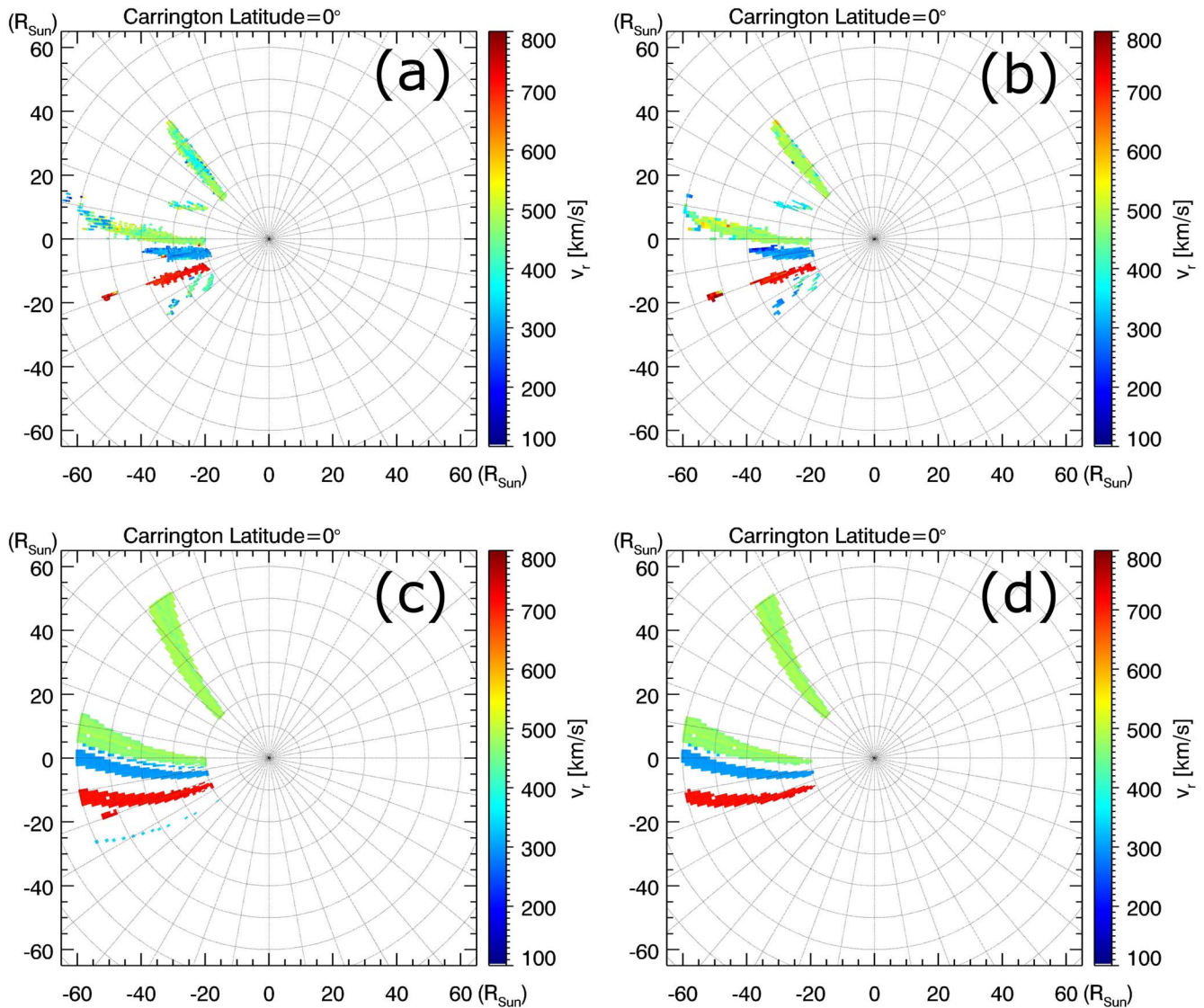
Figure 2. Synoptic solar wind velocity map reconstruction procedures (see Section 3.1). It comes from the reconstruction of the test of synthetic images in the test (see Section 3.2) on the equatorial plane, and the color represents the radial velocity value. The panels represent the derived ST's position distribution after procedure 1 (panel (a)), the velocity map at the grids after data sampling of procedure 2 (panel (b)), after the data smoothing and extension of procedure 3 (panel (c)), and after the data denoising process of procedure 3 (panel (d)).

4.1. Comparison with the Magnetic Neutral Line at 2.5 $R_\odot$

For the spatial distribution of the origins of STs, Plotnikov et al. (2016) found a rare occurrence of the corotating density structures on the ecliptic plane far from the neutral line. To check if it is true for all of the STs recognized in this CR, we extrapolate the synoptic solar wind velocity map to a heliocentric distance of 2.5 $R_\odot$ along the Parker spirals by using the same technique described in the Appendix.

Figure 5(a) shows the locations of the STs, the magnetic field neutral line (corresponding to the HCS from the Wilcox Solar Observatory source surface synoptic charts; Hoeksema et al. 1983), and the contours of the angular distances from the neutral line in the angular space. At a similar angular distance to the HCS, the ST radial velocity between 20 and 60 $R_\odot$ varies a lot at different Carrington longitudes, suggesting a typical angular spatial difference of the solar wind acceleration process. The distribution of the angular distance, $\delta\theta$, between the STs and the neutral line at 2.5 $R_\odot$ is shown in Figure 5(b). The frequency decreases quickly with increasing angular

distance, and the angular distance of the half-maximum is within $10°$, well in agreement with that from Plotnikov et al. (2016). In comparison, we also simulate the distribution of the angular distance by uniformly randomizing the ST locations in the full angular space (shown by the blue diamonds in Figure 5(b)). It can be found that the distribution is much more flattened than the real one. The angular distance of the half-maximum is about $40°$.

At different ranges of $\delta\theta$, the mean value of the ST radial velocity between 20 and 60 $R_\odot$ is calculated and shown in Figure 5(c). Statistically, the radial velocity stays around 300 km s^{-1} at $\delta\theta$ between $5°$ and $20°$. It is tens of kilometers per second larger at the HCS with a $\delta\theta$ of less than $5°$, probably related to the magnetic reconnection at the tips of the helmet streamer (Sanchez-Diaz et al. 2017b; Réville et al. 2022). As $\delta\theta$ rises from $20°$ to $45°$, the radial velocity keeps increasing from nearly 300 to about 400 km s^{-1}, maybe influenced by the fast solar wind far away from the HCS.
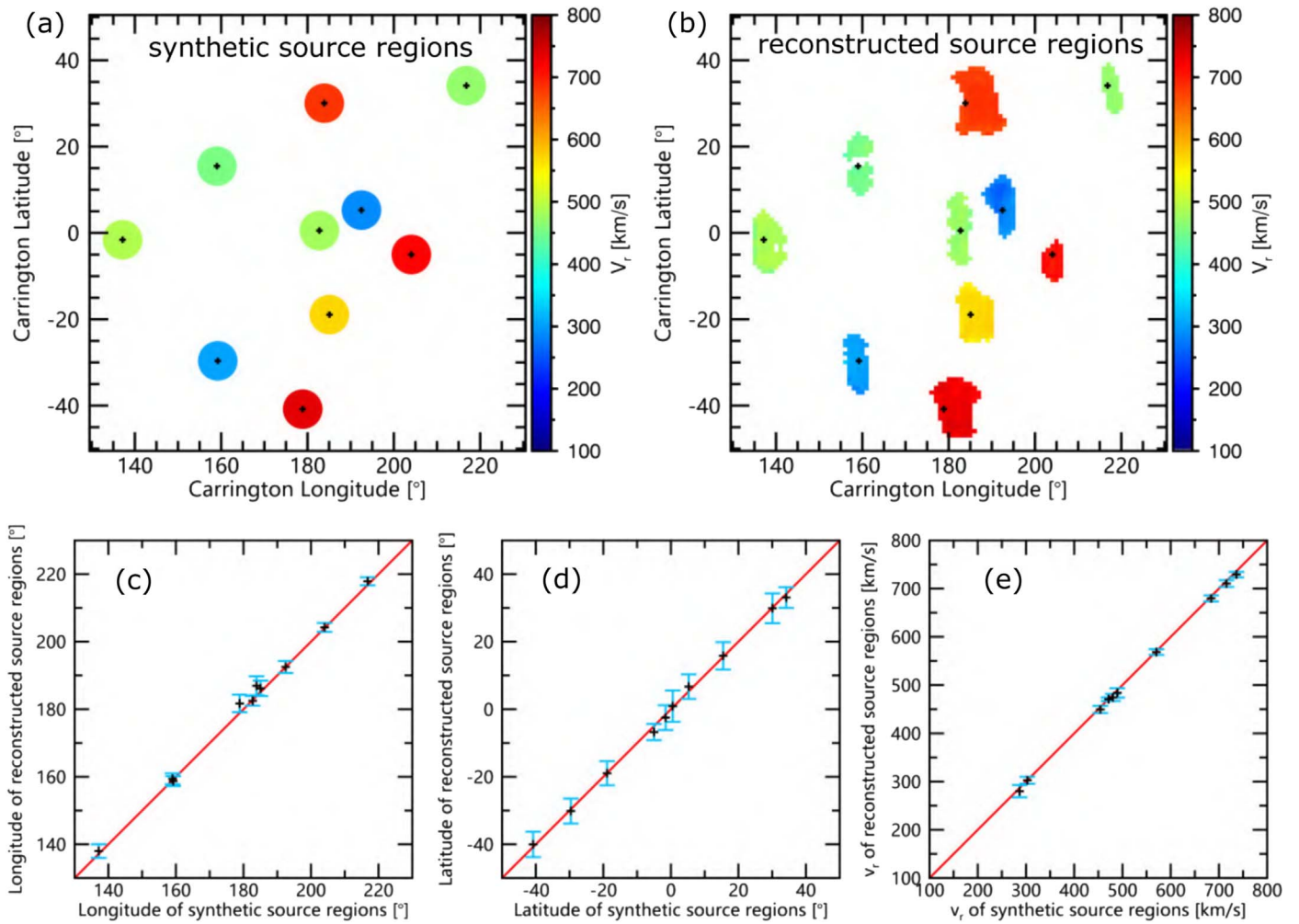
Figure 3. Comparison of synthetic and reconstructed source regions of small-scale transients in the synoptic solar wind velocity map in the test. (a) Angular distribution of synthetic source regions. (b) Angular distribution of reconstructed source regions. In panels (a) and (b), the color of the source regions represents the corresponding transients' velocity (v_r). (c)–(e) Comparison of synthetic and reconstructed source regions in Carrington longitude, Carrington latitude, and transient velocity (v_r). Black plus signs and blue error bars mark the mean and standard deviation of the corresponding parameters for the reconstructed source regions. The red line indicates that the parameters of the synthetic and reconstructed source regions are equal in value.

4.2. Comparison with In Situ Observations Near 1 au

To check the reliability of the reconstructed synoptic solar wind velocity map, we compare it with solar wind velocity observations from the Wind spacecraft near the Sun–Earth Lagrange 1 point and two STEREO spacecraft. We sample the median value of the in situ observed solar wind radial velocity component, proton density, and temperature per hour recorded by the Plasma and Suprathermal Ion Composition investigation (Galvin et al. 2008) on board STEREO-A/B (see Figures 6(b), (c), (e), and (f)) and the Solar Wind Experiment (Ogilvie et al. 1995) on board Wind (see Figures 6(h) and (i)). The same process is applied to the magnetic field magnitude, component, and polarity detected by the In situ Measurements of Particles And CME Transients (Luhmann et al. 2008) on board STEREO-A/B (see Figures 6(d) and (g)) and the Wind Magnetic Field Investigation of the Wind spacecraft (Lepping et al. 1995; see Figure 6(j)). Based on these sampling data, we calculate the plasma beta value per hour (green points in Figures 6(c), (f), and (i)). According to the median value of the in situ observed solar wind radial velocity per hour, we extrapolate the location of the current spacecraft along the associated Parker spiral to a heliocentric distance of 20 $R_\odot$ to

find the corresponding radial velocity obtained in our synoptic solar wind velocity map at 20 $R_\odot$ (see Figure 6(a)). The found velocity points are displayed as orange points in Figures 6(b), (e), and (f).

For convenience, we put the scattered velocity points into groups, as indicated by the shaded regions in Figures 6(b)–(j). The detailed comparison results and associated solar wind structures for each group are listed in Table 1. Half of the groups (7 of 14) correspond to the heliospheric plasma sheet (HPS; Winterhalter et al. 1994) in the in situ observations with a high plasma beta value, high proton density, low temperature, and magnetic radial component polarity reversal, and they all correspond to a small velocity bias (<40 km s^{-1}). Five groups meet the flux rope (with a low plasma beta value, low temperature, low plasma density, and high magnetic field strength), and four of them also meet the solar wind compression region (with a high plasma beta value, high temperature, and high plasma density) ahead of the flux rope. One group meets the fast wind part of the corotating interaction region (CIR; with a slow solar wind velocity increase, high plasma density, high temperature, and high magnetic field
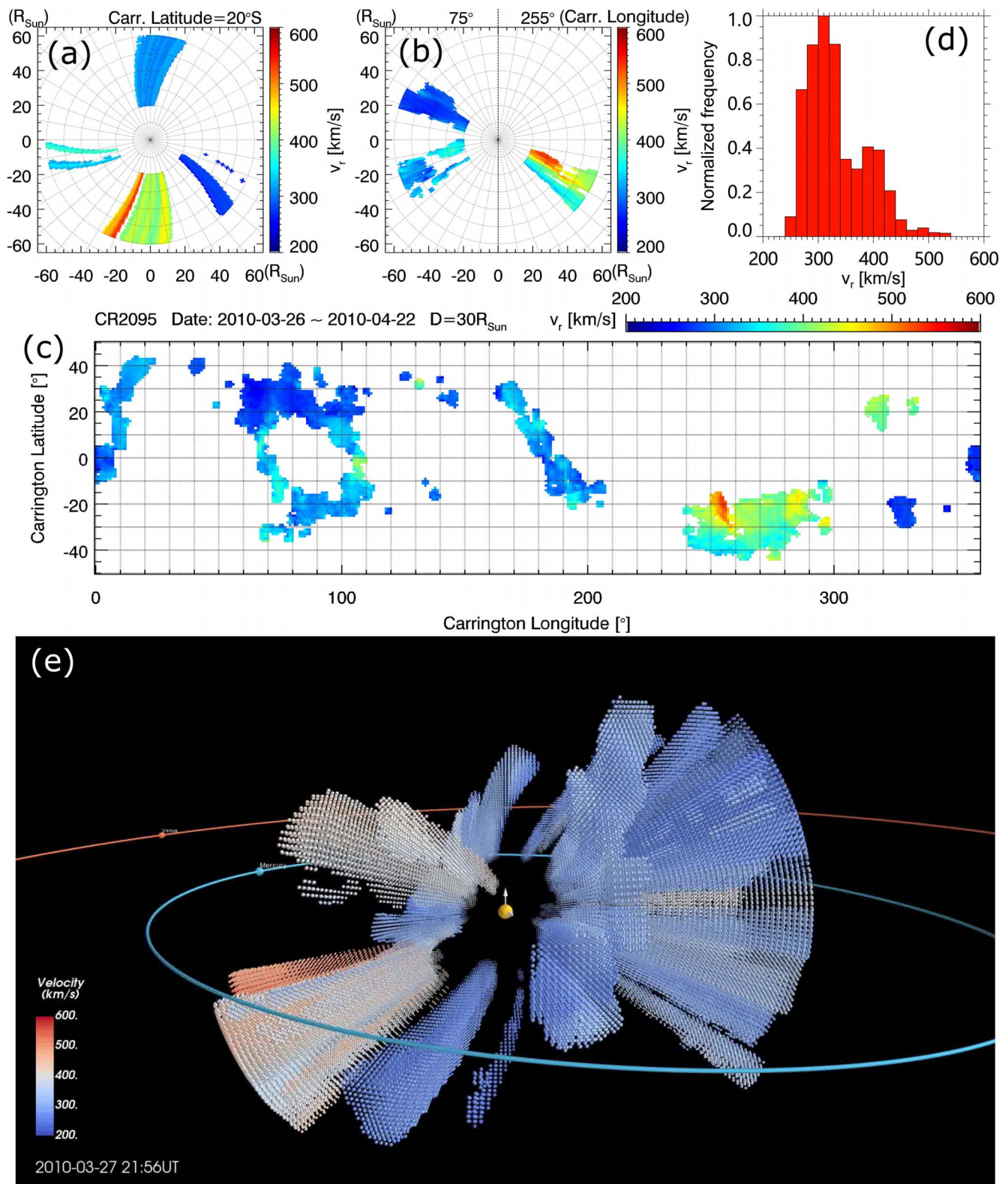
Figure 4. Reconstructed synoptic solar wind velocity map for STEREO HI1 images during CR 2095. (a) Velocity distribution on the colatitudinal plane of 20°S. (b) Velocity distribution on the meridian plane with a latitude of 75° on the east and 255° on the west. (c) Velocity distribution on the sphere with the same heliocentric distance of 30 $R_\odot$. (d) Normalized frequency distribution of radial velocity (v_r). (e) Synoptic solar wind velocity map of CR 2095 in 3D space in Carrington coordinates at 21:56 UT on 2010 March 27. The grids with a valid solar wind velocity are marked as small balls, with the color representing the local velocity value in the synoptic map. We also mark the positions of the Sun (big yellow ball at the center), Mercury (blue ball), and Venus (orange ball), along with their orbits. A corresponding animation of panel (e) is provided in the online journal. It covers about 27 days in CR 2095 from 11:44 UT on 2010 March 26 to 09:56 UT on 2010 February 22. The video duration is 28 s.

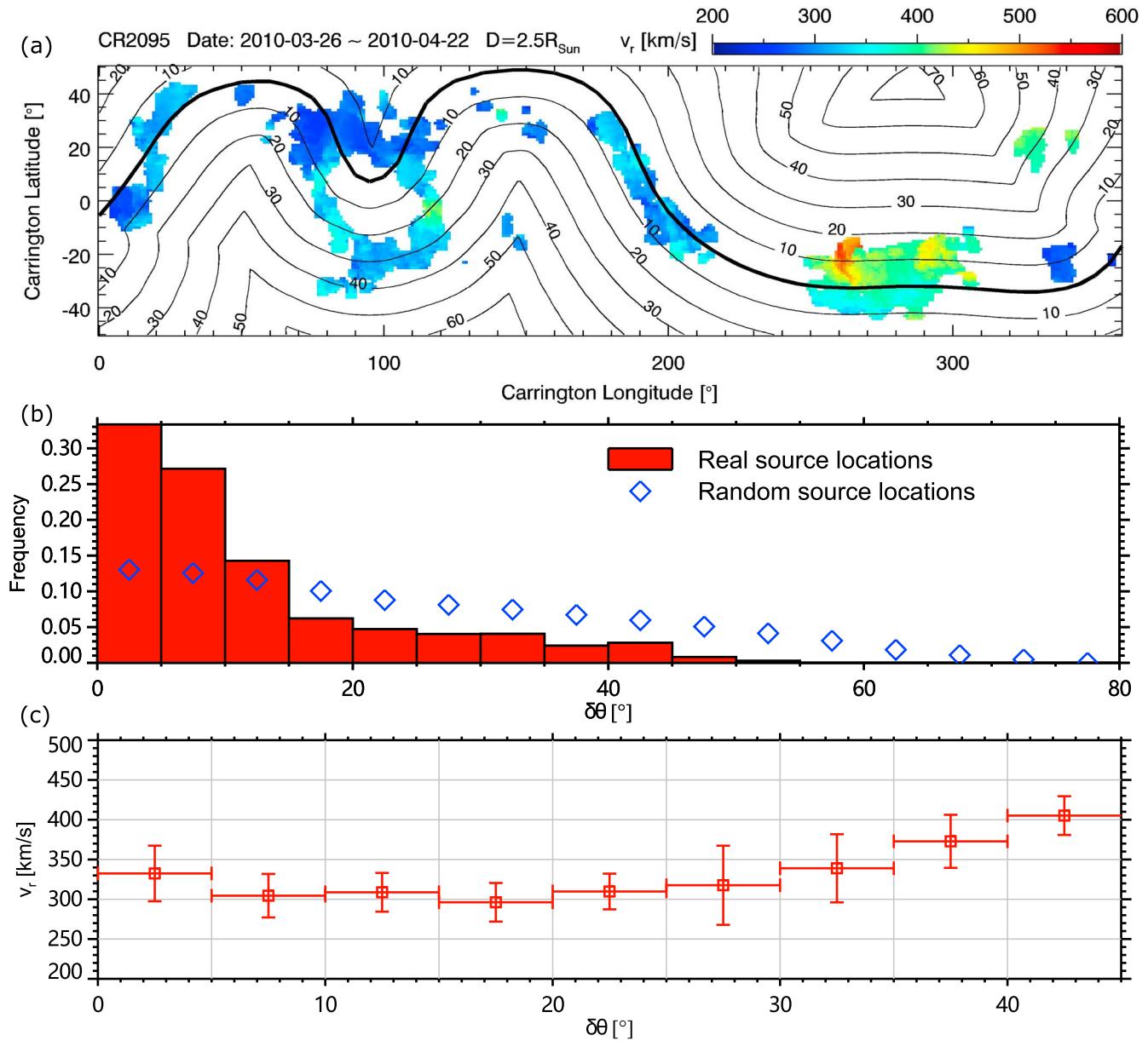(An animation of this figure is available.)

Figure 5. Synoptic solar wind velocity map extrapolated to a heliocentric distance of 2.5 $R_\odot$ along the Parker spiral. (a) Contour of $\delta\theta$, the minimum distance to the magnetic neutral line in angular space at 2.5 $R_\odot$ on the extrapolated synoptic solar wind velocity map. The thick black curves represent the positions of the magnetic neutral line at 2.5 $R_\odot$ from Wilcox Solar Observatory source surface synoptic charts. (b) Frequency distribution of $\delta\theta$ at 2.5 $R_\odot$ for the extrapolated synoptic solar wind velocity map. The blue diamonds represent the frequency in the situation of uniformly randomizing ST locations in the full angular space. (c) Mean value of the radial solar wind velocity in the extrapolated synoptic solar wind velocity map at different ranges of $\delta\theta$ at 2.5 $R_\odot$. The horizontal and vertical error bars represent the range of $\delta\theta$ and the standard deviation of the velocity value.

strength during the velocity increase), and the last one is in a slow solar wind stream.

We find that the velocity differences between the in situ observations and the synoptic solar wind velocity map of most of the groups are larger than zero (see Table 1), suggesting the acceleration of the solar wind in the inner heliosphere. The HPS and slow stream–associated groups generally have a smaller velocity difference than the other groups, which implies that our extrapolation may have a larger deviation when other disturbed structures, e.g., CIRs or CMEs, are present. Without considering the STs caught up by CIRs or CMEs, the average radial solar wind velocity deviation between them is only 23 ± 39 km s^{-1}, suggesting that the radial solar wind velocity

from the synoptic solar wind velocity map matches well with in situ observations.

4.3. Comparison with Solar Wind Simulations

We compare our synoptic radial solar wind velocity map with the simulations of CR 2095 by the ENLIL model (Odstrcil 2003) and improved IN-TVD model (Shen et al. 2018). Both models use the Wang–Sheely–Arge empirical model (Wang & Sheeley 1990; Arge et al. 2003) to derive the inner boundary solar wind condition at about 0.1 au based on a magnetogram provided by the Global Oscillation Network Group project. The computational domain covers [0°, 360°] in longitude, [−60°, 60°]/[−90°, 90°] for the ENLIL/IN-TVD model in latitude, and [22, 365 $R_\odot$]/[21.5, 258 $R_\odot$] for the
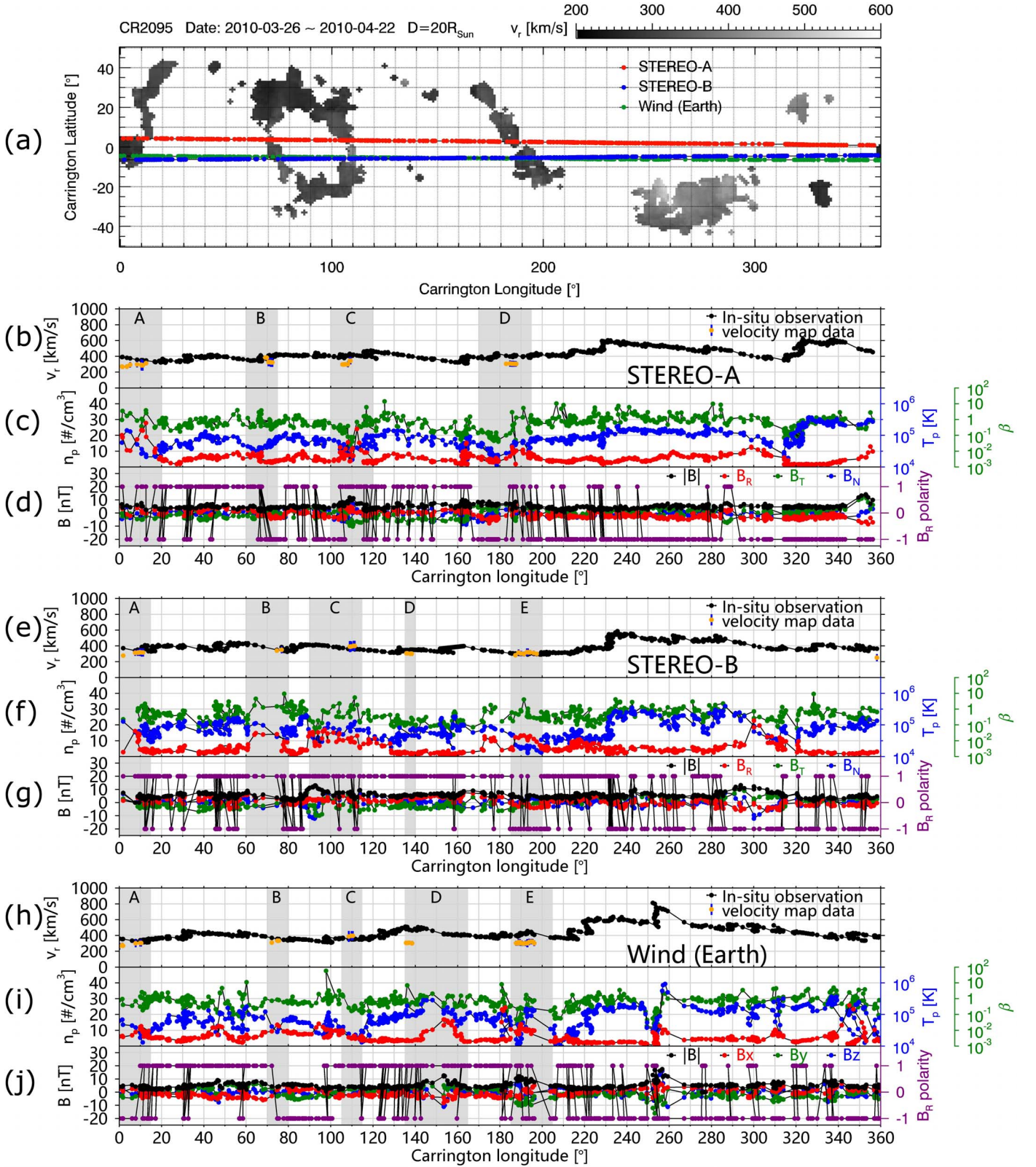
Figure 6. Comparison of the synoptic solar wind velocity map at 20 $R_{\odot}$ and the solar wind in situ observation from STEREO-A (panels (b)–(d)), STEREO-B (panels (e)–(g)), and the Wind spacecraft (panels (h)–(j)) extrapolated to 20 $R_{\odot}$ along the Parker spiral. (a) Angular position of STEREO-A (red), STEREO-B (blue), and the Wind spacecraft (green) extrapolated to 20 $R_{\odot}$ and the synoptic solar wind velocity map during CR 2095. (b), (e), and (h) Comparison of the in situ observed solar wind radial velocity (black) and corresponding velocity (orange) with its error (blue) in the synoptic velocity map. (c), (f), and (i) In situ observed solar wind proton number density n_p (red), proton temperature T_p (blue), and plasma beta value β (green). (d), (g), and (j) In situ observed local magnetic field, including total magnetic field strength $|B|$ (black); components B_R (red), B_T (green), and B_N (blue) in the radial–tangential–normal coordinate system for STEREO or B_x (red), B_y (green), and B_z (blue) in the geocentric solar ecliptic coordinate system for Wind; and radial component polarity (purple). The shaded regions represent different groups labeled A to E for velocity comparison.

Table 1
Comparison of the Synoptic Solar Wind Velocity Map at 20 $R_\odot$ and Solar Wind In Situ Observations from STEREO-A, STEREO-B, and Wind Extrapolated to 20 $R_\odot$ along the Parker Spiral for Each Group

Spacecraft	Group	Longitude (deg)	Latitude (deg)	$v_{\text{in situ}}$ (km s^{-1})	v_{map} (km s^{-1})	$\delta v = v_{\text{in situ}} - v_{\text{map}}$ (km s^{-1})	Associated Structure[a]
STA	A	[0, 20]	4.3N	$364^{\pm19}$	$289^{\pm17}$	$75^{\pm34}$	HPS
STA	B	[60, 75]	3.7N	$382^{\pm18}$	$333^{\pm21}$	$49^{\pm32}$	HPS
STA	C	[100, 120]	3.3N	$403^{\pm16}$	$307^{\pm19}$	$96^{\pm17}$	CR+FR
STA	D	[170, 195]	2.6N	$404^{\pm7}$	$305^{\pm1}$	$99^{\pm8}$	CR+FR
STB	A	[0, 15]	6.4S	$349^{\pm16}$	$311^{\pm12}$	$37^{\pm23}$	HPS
STB	B	[60, 80]	6.1S	$367^{\pm25}$	$345^{\pm7}$	$21^{\pm17}$	HPS
STB	C	[90, 115]	5.9S	$363^{\pm6}$	$394^{\pm4}$	$-32^{\pm8}$	CR+FR
STB	D	[135, 140]	5.8S	$349^{\pm3}$	$303^{\pm3}$	$46^{\pm5}$	SS
STB	E	[185, 200]	5.5S	$298^{\pm5}$	$312^{\pm12}$	$-13^{\pm13}$	HPS
Wind	A	[0, 15]	4.6S	$342^{\pm14}$	$289^{\pm18}$	$52^{\pm32}$	HPS
Wind	B	[70, 80]	5.1S	$361^{\pm8}$	$325^{\pm14}$	$35^{\pm22}$	HPS
Wind	C	[105, 115]	5.3S	$352^{\pm3}$	$393^{\pm5}$	$-41^{\pm8}$	FR
Wind	D	[135, 165]	5.6S	$483^{\pm18}$	$305^{\pm3}$	$178^{\pm17}$	CIR
Wind	E	[185, 205]	5.9S	$418^{\pm17}$	$307^{\pm8}$	$110^{\pm18}$	CR+FR

Note.
[a] CR: compression region; FR: flux rope; SS: slow stream.

ENLIL/IN-TVD model in heliocentric distance. The longitudinal and latitudinal grid size is 1°, and the radial grid size is 0.34 $R_\odot$ for the ENLIL model or [0.37, 2.37 $R_\odot$] from the inner to the outer boundary for the IN-TVD model.

Figure 7 shows the comparison at 30 $R_\odot$. It is found that the simulated velocity (v_r^{sim}) is generally larger than our derived velocity (v_r^{map}). For ENLIL, the difference ($\delta v_r = v_r^{\text{sim}} - v_r^{\text{map}}$) is hundreds of kilometers per second, and for IN-TVD, the difference is roughly less than 100 km s^{-1}. The distributions of v_r^{sim}, v_r^{map}, and δv_r as a function of $\delta\theta$ for the two models are displayed in Figures 7(d) and (h). We find that near the HCS ($\delta\theta < 10°$), the simulation results from the two models are most consistent with the synoptic map. However, the δv_r from the ENLIL model increases notably as $\delta\theta$ increases. The situation of IN-TVD is much better. This suggests that the ENLIL and IN-TVD models are valid in the region close to the magnetic field neutral line, i.e., the HCS. In the region far away from the HCS, where the fast solar wind normally dominates in the simulations, we can still detect some STs, mainly in the slow wind, which the simulations could not reconstruct. This is probably the reason for the large absolute δv_r value at large $\delta\theta$.

5. Summary and Concluding Remarks

Based on the STEREO-A/B HI1 images of STs in a solar rotation, we developed a technique to make a synoptic solar wind radial velocity map of latitude between 50°S and 50°N, longitude between 0° and 360°, and heliocentric distance between 20 and 60 $R_\odot$. The test with synthetic images suggests that the synoptic velocity map recovers the preset synthetic blobs in latitude, longitude, and velocity fairly well. By applying the method to the STEREO HI1 images during CR 2095, we successfully generate the synoptic velocity map, though the 3D space is not fully covered. We find that most of the reconstructed solar wind belongs to the slow wind (<500 km s^{-1}), with two distribution peaks at 310 and 400 km s^{-1}. They may relate to different kinds of solar wind origins or acceleration mechanisms. Besides, there are also STs with a radial velocity of over 500 km s^{-1} at a Carrington latitude of around 20°S and longitude of around 225°, as shown in

Figure 4(c). We analyzed the corresponding STs before (i.e., blob 2 on April 4 in Paper II) and considered it as the result of blob–blob interaction.

These reconstructed STs mainly originate from a thick layer surrounding the HCS with an angular distance of less than 10°, consistent with the theory that the slow solar wind originates from the dynamic interface layers as an open–closed magnetic field boundary with an angular extent of approximately 40° around the HCS (Antiochos et al. 2011). We also find that the radial solar wind velocity from the synoptic map matches well with in situ observations from Wind and STEREO-A/B near 1 au. Half of the compared solar winds are associated with the HPS, and the average radial solar wind velocity deviation between them is only 23 ± 39 km s^{-1}. A larger deviation between the inferred velocity and in situ observations is associated with the disturbed solar wind, e.g., CIRs or CMEs.

Further, the comparison of the synoptic map with two numerical models, ENLIL and improved IN-TVD, suggests that both models match well with the synoptic map near the HCS with an angular distance of no more than 10°. However, at a far distance from the HCS, the radial velocity in both simulations is generally much larger than that in the synoptic map. The ENLIL model deviates from our results much more than the IN-TVD model, which may imply that ENLIL may miss more slow wind components in the region away from the HCS.

The technique developed in this paper will be a powerful tool to reveal the solar wind velocity distribution in the 3D inner heliosphere as long as there are suitable dual-view imaging observations with a longitudinal separation angle between 120° and 150° (Lyu et al. 2021), like that provided by STEREO in the first half of 2010. Due to the loss of communication of STEREO-B in 2014, we cannot derive the velocity map based on two STEREO HI1 images after 2014. However, the recent Wide-field Imager for Solar PRobe of PSP (Vourlidas et al. 2016) and SoloHI on board the Solar Orbiter (Howard et al. 2020; Müller et al. 2020) may take on the role of STEREO-B in constructing the synoptic solar wind velocity map after 2018. In particular, the technique will show its value
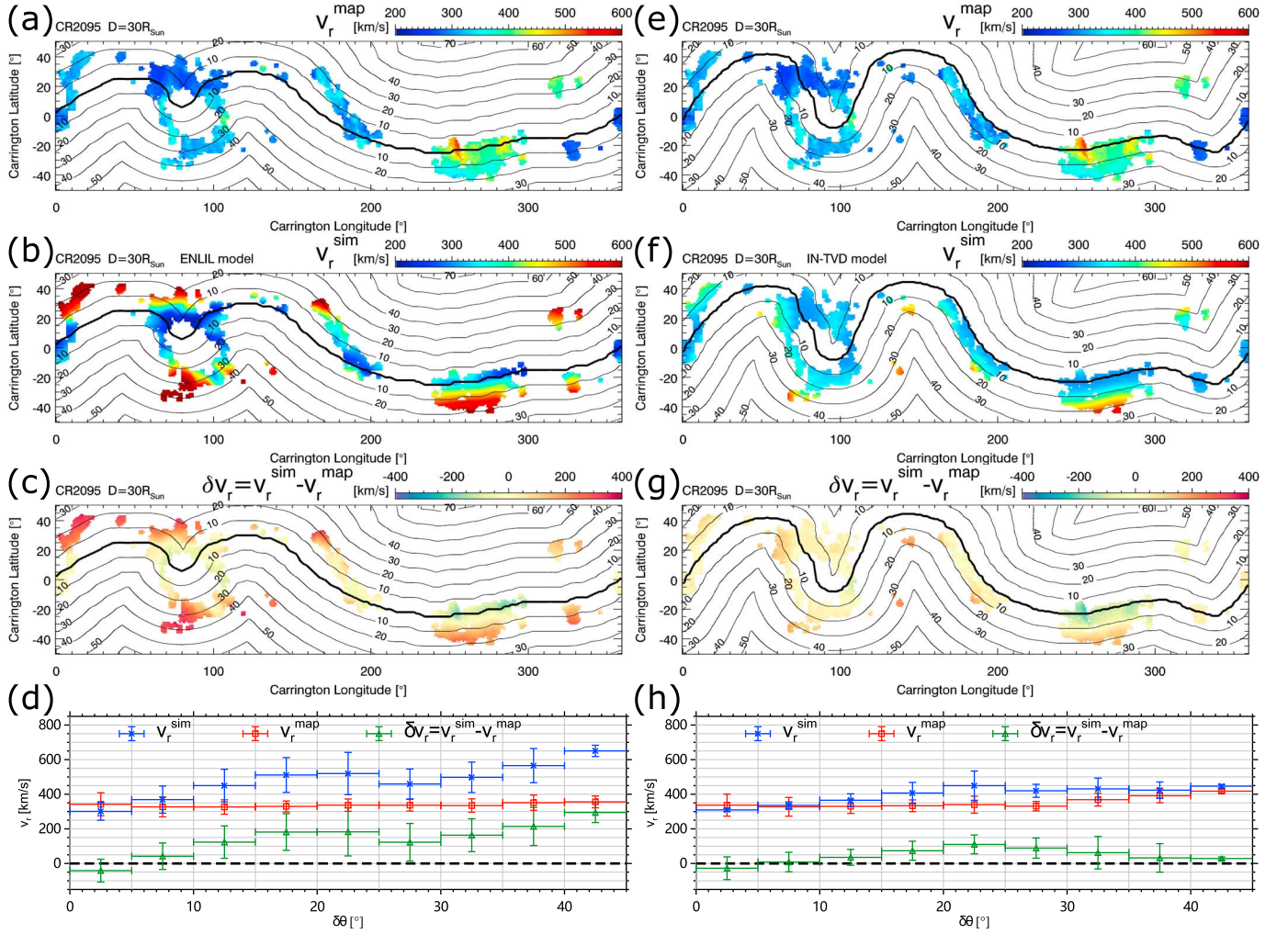
Figure 7. Comparison of the solar wind radial velocity from the synoptic solar wind velocity map and simulation of the ENLIL model (panels (a)–(d)) or improved IN-TVD model (panels (e)–(h)) at 30 $R_\odot$. (a) and (e) Angular distribution of v_r^{map}, the radial solar wind velocity in the synoptic solar wind velocity map. (b) and (f) Angular distribution of v_r^{sim}, the radial solar wind velocity in the simulation in the same angular position as v_r^{map}. (c) and (g) Angular distribution of $\delta v_r = v_r^{sim} - v_r^{map}$. The contour of $\delta\theta$, the minimum distance to the HCS (thick black curve) in angular space, is displayed in panels (a)–(c) for the ENLIL model and panels (e)–(g) for the improved IN-TVD model. (d) and (h) Mean value of v_r^{sim} (blue), v_r^{map} (red), and δv_r (green) at different ranges of $\delta\theta$. The horizontal and vertical error bars represent the range of $\delta\theta$ and the standard deviation of the velocity value.

in future multisatellite space missions, such as the Solar Ring mission (Wang et al. 2020, 2023) or the L4–L5 mission (Bemporad 2021). Besides, this technology can also be extended to coronagraph images, from which the synoptic radial velocity map at a lower height in the corona ($<20\ R_\odot$) may be obtained.

Appendix
Data Smoothing, Extension, and Denoising Process

In Section 3.1, during procedure 3, to make sure the synoptic velocity map is continued and smoothed along the Parker spiral, we have to reset the velocity at each grid point; we call

this process "data smoothing and extension," which includes four steps.

Step 1. At a certain grid point p, we set the initial velocity, $v_i^{l,p}$, where l is the loop number. If there are valid velocity data, v_s, sampled, then $v_i^{0,p}$ equals v_s; if not, we set $v_i^{0,p}$ as 300 km s^{-1}, the general ST velocity in the inner heliosphere (Plotnikov et al. 2016).

Step 2. We search all of the grid points along the corresponding Parker spiral with a valid radial velocity sampled ($v_i^{l,p}$) and passing the object grid point p. Then, we derive the sampled velocity list $v_s^{l,k,p}$ and the list of its deviation $\delta v_s^{l,k,p}$, $k = 1, 2, \ldots, n$, where l is the loop number, and n is the number of grid points in the list. The longitude and heliocentric distance (ϕ, r) of the Parker spiral curve satisfy

$$\phi(r) = \phi^p - \frac{\Omega_\odot}{v_i^{l,p}}(r - r^p), \tag{A1}$$

where ϕ^p and r^p are the longitude and heliocentric distance of point p, and $\Omega_\odot$ is the solar rotation rate of $2\pi/27.2753$ days in Carrington coordinates.

Step 3. If n is too small (<8), we think that there is too little information to derive the velocity here, so we regard the velocity data to be invalid at the grid point p. On the contrary, with more grid points in the list ($n \geqslant 8$), we calculate the weight as $w^{l,k,p}$, $k = 1, 2, \ldots, n$, as Equation (A2) shows, and use it to derive the weighted average velocity $v_i^{l+1,p}$ and its deviation $\delta v_i^{l+1,p}$, as Equations (A3) and (A4) show:

$$w^{l,k,p} = \frac{\frac{1}{\max(\delta v_s^{l,k,p}, 10 \ \mathrm{km \ s}^{-1})}}{\sum_{k=1}^{n}\frac{1}{\max(\delta v_s^{l,k,p}, 10 \ \mathrm{km \ s}^{-1})}}, \tag{A2}$$

$$v_i^{l+1,p} = \sum_{k=1}^{n} w^{l,k,p} v_s^{l,k,p}, \tag{A3}$$

$$\delta v_i^{l+1,p} = \sqrt{\sum_{k=1}^{n} w^{l,k,p}(v_s^{l,k,p} - v_i^{l+1,p})^2}. \tag{A4}$$

If $|v_i^{l+1,p} - v_i^{l,p}| \geqslant 1$ km s^{-1}, we continue the circulation and go back to step 1 with $v_i^{l+1,p}$ as the new initial velocity. If $|v_i^{l+1,p} - v_i^{l,p}| < 1$ km s^{-1}, we finish the loop and go to step 4.

Step 4. After the lth loop, if $\delta v_i^{l+1,p}$, the absolute deviation of $v_i^{l+1,p}$, is too large (>60 km s^{-1}) or $\delta v_i^{l+1,p}/v_i^{l+1,p}$, the relative deviation of $v_i^{l+1,p}$, is too large (>0.3), the result is considered to be invalid. Otherwise, we think that $v_i^{l+1,p}$ at the grid point p is reliable and treat it as the value of the local solar wind velocity, v_o^p. After dealing with all of the grid points with steps 1–4, we derive the 3D v_o matrix as the result of the data smoothing and extension.

After the data smoothing and extension process (see Figure 2(c) for results), there are also tiny isolated structures as probable noise in the velocity map. To eliminate them, we do a simple binarization by building the flag matrix F_o with a value of 1 at the grids with a valid value of v_o and zero at other grid points. Then, we derive a new 3D binary matrix F_n by doing a 3D erosion and dilation on F_o with a $3 \times 3 \times 3$ structure element matrix where the value is zero at the eight corners and 1 at the others. Only at the grids with a value of 1 in F_n do we fill the velocity value, v_r, and build the final velocity map. If the F_o value here is 1 as well, the v_r value here equals the v_o value. Otherwise, we set the v_r value here as the

mean v_o value of the neighboring grid points with an F_o value of 1. The final synoptic velocity map after the data denoising process is displayed in Figure 2(d).

ORCID iDs

Xiaolei Li ⓘ https://orcid.org/0000-0002-7685-1528
Yuming Wang ⓘ https://orcid.org/0000-0002-8887-3919
Fang Shen ⓘ https://orcid.org/0000-0002-4935-6679
Quanhao Zhang ⓘ https://orcid.org/0000-0003-0565-3206
Shaoyu Lyu ⓘ https://orcid.org/0000-0002-2349-7940

References

Antiochos, S. K., Mikić, Z., Titov, V. S., Lionello, R., & Linker, J. A. 2011, ApJ, 731, 112
Arge, C. N., Odstrcil, D., Pizzo, V. J., & Mayer, L. R. 2003, in AIP Conf. Ser. 679, Solar Wind Ten, ed. M. Velli et al. (Melville, NY: AIP), 190
Bemporad, A. 2021, FrASS, 8, 11
Capuano, G. E., Dolei, S., Spadaro, D., et al. 2021, A&A, 652, A85
Cho, I.-H., Moon, Y.-J., Nakariakov, V. M., et al. 2018, PhRvL, 121, 075101
Crooker, N. U., Antiochos, S. K., Zhao, X., & Neugebauer, M. 2012, JGRA, 117, A04104
DeForest, C. E., Howard, R. A., Velli, M., Viall, N., & Vourlidas, A. 2018, ApJ, 862, 18
DeForest, C. E., Matthaeus, W. H., Viall, N. M., & Cranmer, S. R. 2016, ApJ, 828, 66
Dolei, S., Susino, R., Sasso, C., et al. 2018, A&A, 612, A84
Eyles, C. J., Harrison, R. A., Davis, C. J., et al. 2009, SoPh, 254, 387
Galvin, A. B., Kistler, L. M., Popecki, M. A., et al. 2008, SSRv, 136, 437
Harrison, R. A., Davis, C. J., Eyles, C. J., et al. 2008, SoPh, 247, 171
Hoeksema, J. T., Wilcox, J. M., & Scherrer, P. H. 1983, JGR, 88, 9910
Hollweg, J. V., & Isenberg, P. A. 2002, JGRA, 107, 1147
Howard, R. A., Moses, J. D., Vourlidas, A., et al. 2008, SSRv, 136, 67
Howard, R. A., Vourlidas, A., Colaninno, R. C., et al. 2020, A&A, 642, A13
Jackson, B. V., Hick, P. L., Kojima, M., & Yokobe, A. 1998, JGR, 103, 12049
Kasper, J. C., Abiad, R., Austin, G., et al. 2016, SSRv, 204, 131
Lepping, R. P., Acũna, M. H., Burlaga, L. F., et al. 1995, SSRv, 71, 207
Li, X., Wang, Y., Guo, J., Liu, R., & Zhuang, B. 2021, A&A, 649, A58
Li, X., Wang, Y., Liu, R., et al. 2020, JGRA, 125, e27513
López-Portela, C., Panasenco, O., Blanco-Cano, X., & Stenborg, G. 2018, SoPh, 293, 99
Luhmann, J. G., Curtis, D. W., Schroeder, P., et al. 2008, SSRv, 136, 117
Lyu, S., Wang, Y., Li, X., et al. 2021, ApJ, 909, 182
McComas, D. J., Ebert, R. W., Elliott, H. A., et al. 2008, GeoRL, 35, L18103
Müller, D., St. Cyr, O. C., Zouganelis, I., et al. 2020, A&A, 642, A1
Odstrcil, D. 2003, AdSpR, 32, 497
Ogilvie, K. W., Chornay, D. J., Fritzenreiter, R. J., et al. 1995, SSRv, 71, 55
Parker, E. N. 1958, ApJ, 128, 664
Plotnikov, I., Rouillard, A. P., Davies, J. A., et al. 2016, SoPh, 291, 1853
Réville, V., Fargette, N., Rouillard, A. P., et al. 2022, A&A, 659, A110
Réville, V., Velli, M., Rouillard, A. P., et al. 2020, ApJL, 895, L20
Rouillard, A. P., Davies, J. A., Lavraud, B., et al. 2010, JGRA, 115, A04103
Sanchez-Diaz, E., Rouillard, A. P., Davies, J. A., et al. 2017a, ApJ, 851, 32
Sanchez-Diaz, E., Rouillard, A. P., Davies, J. A., et al. 2017b, ApJL, 835, L7
Sheeley, N. R., Wang, Y. M., Hawley, S. H., et al. 1997, ApJ, 484, 472
Sheeley, N. R. J., Herbst, A. D., Palatchi, C. A., et al. 2008, ApJL, 674, L109
Shen, F., Yang, Z., Zhang, J., Wei, W., & Feng, X. 2018, ApJ, 866, 18
Stakhiv, M., Lepri, S. T., Landi, E., Tracy, P., & Zurbuchen, T. H. 2016, ApJ, 829, 117
Tokumaru, M., Fujiki, K., Kojima, M., & Iwai, K. 2021, ApJ, 922, 73
Viall, N. M., Spence, H. E., Vourlidas, A., & Howard, R. 2010, SoPh, 267, 175
Viall, N. M., & Vourlidas, A. 2015, ApJ, 807, 176
Vourlidas, A., Howard, R. A., Plunkett, S. P., et al. 2016, SSRv, 204, 83
Wang, Y., Bai, X., Chen, C., et al. 2023, AdSpR, 71, 1146
Wang, Y., Ji, H., Wang, Y., et al. 2020, ScChE, 63, 1699
Wang, Y. M., & Sheeley, N. R. J. 1990, ApJ, 355, 726
Winterhalter, D., Smith, E. J., Burton, M. E., Murphy, N., & McComas, D. J. 1994, JGR, 99, 6667
Ying, B., Bemporad, A., Giordano, S., et al. 2019, ApJ, 880, 41